Solid Freeform Fabrication 2024: Proceedings of the 35th Annual International Solid Freeform Fabrication Symposium – An Additive Manufacturing Conference
Reviewed Paper

Effect of Heat Treatment on the Micro-/Defect-structure and Tensile Behavior of Additively Manufactured A6061-RAM2 Aluminum Alloy

Md Faysal Khan[1,2], Reza Ghiaasiaan[1,2], Paul R. Gradl[3], Samad Firdosy[4], Shuai Shao[1,2], Nima Shamsaei[1,2*]

[1]National Center for Additive Manufacturing Excellence (NCAME), Auburn University, Auburn, AL 36849, USA

[2]Department of Mechanical Engineering, Auburn University, Auburn, AL 36849, USA

[3]Propulsion Department, NASA Marshall Space Flight Center, Huntsville, Al 35812, USA

[4]NASA Jet Propulsion Laboratory, California Institute of Technology Pasadena, CA 91011, USA

* Corresponding author:

Email: shamsaei@auburn.edu

Tel: (334) 844 4839

Abstract

This study investigated the effect of heat treatment (HT) on micro-/defect-structure and room temperature tensile behavior of A6061-RAM2 alloy fabricated using laser powder bed fusion (L-PBF). Specimens were fabricated via reactive additive manufacturing powder and process, using a mixture of TiC and B_4C inoculant particles into pre-alloyed A6061 powder. This process resulted in a crack-free, grain-refined metal matrix composite. These particles acted as grain boundary pinners and facilitated the formation of equiaxed grains. The effect of different HT operations post-build, including hot isostatic pressing (HIP), solutionizing, and aging, conducted at varying temperatures and durations were examined. All HTs incorporating HIP greatly reduced defect content compared to the non-heat treated condition but had minimal impact on the grain structure of the alloy. The alloy showed noticeable changes in tensile properties with variations in solutionizing (at 500-530 °C for 1.5-2 hrs) and aging (at 160-180 °C for 8-34 hrs) temperature and duration. Tensile strengths increased with longer aging durations due to more efficient Mg_2Si precipitation.

Keywords: Laser powder bed fusion (L-PBF), A6061-RAM2, Heat treatment, Micro-/defect-structure, Tensile behavior

Introduction

A6061, a widely used heat-treatable Al-Si-Mg alloy, finds applications across various industries such as transportation, construction, aerospace, automotive, marine, appliances, gas and air cylinders, and food packaging [1][2]. Its popularity stems from its medium strength, formability, machinability, corrosion resistance, high strength-to-weight ratio, and low cost [3][4]. Additive manufacturing (AM), e.g., laser powder bed fusion (L-PBF), enhances the applicability of A6061 by enabling the integration of complex thin or internal features, reduction in manufacturing time and cost, lattice structures, and other complex geometry, which are often challenging with conventional manufacturing methods [5][6].

A6061 presents challenges in fabrication using L-PBF due to its high crack sensitivity during solidification [7][8]. Literature extensively discusses the formation of solidification cracks in Al-Si-Mg alloy systems for different welding processes [9][10]. A key factor contributing to solidification cracking is the significant difference between the solidus (at 576-585 °C) and liquidus (at 640-652 °C) temperatures of the alloy [11]. This difference leads to the formation of an extensive dendritic network in the mushy zone, delaying liquid flow processes to the shrinkage regions [12][13]. Additionally, the absence of a certain eutectic point and the influence of liquid metal surface tension further exacerbate the issue [14].

Elementum 3D developed a patented method to fabricate A6061 alloy, addressing solidification cracking by introducing inoculant particles as grain refiners. This innovative approach yields an improved microstructure and comparable mechanical characteristics to the wrought alloy [15][16]. By incorporating 2% TiC and B_4C inoculant particles mixed within the pre-alloyed A6061 powder and utilizing a reactive additive manufacturing (RAM) strategy, Elementum 3D successfully produce a crack-free, grain-refined, dispersion-strengthened metal matrix composite (MMC) known as A6061-RAM2 alloy. While A6061 is typically subjected to a T6 heat treatment (HT) after AM or conventional manufacturing processes to enhance strength through precipitation strengthening [17], the effect of HT on A6061-RAM2 alloy is not well understood in the literature. Therefore, this study aims to examine the effect of HT on the microstructure, defect content, and room temperature tensile behavior of A6061-RAM2 alloy fabricated via L-PBF.

Experimental Procedure

The specimens were fabricated using gas-atomized A6061-RAM2 powders supplied by Elementum 3D. The powder particle size range was 13-63 μm, with D_{10} = 13.7 μm, D_{50} = 32.2 μm, and D_{90} = 57.9 μm (representing the 10^{th}, 50^{th}, and 90^{th} size percentiles, respectively). The chemical composition of the powder, measured using inductively coupled plasma-optical emission spectrometry (ICP-OES) by the supplier, is listed in **Table 1**.

Table 1. Chemical composition of A6061-RAM2 powder, supplied by Elementum 3D, measured via ICP-OES.

Element	**Al**	**B**	**C**	**Ti**	**Cu**	**Mg**	**Si**	**Fe**	**Zn**
(wt.%)	Bal.	0.72	0.23	3.04	0.26	0.89	0.66	0.15	0.01
Element	**Cr**	**Ni**	**O**	**N**					
(wt.%)	0.09	0.01	0.04	<0.01					

Cylindrical coupons measuring 12 mm in diameter and 50 mm in length, and thin-wall tensile specimens measuring 12 mm in width, 3 mm in thickness, and 80 mm in length were fabricated vertically via L-PBF using the EOS M290 machine. The following process parameters were used for fabrication: laser power of 370 W, scanning speed of 1400 mm/s, hatch spacing of 200 μm, and layer thickness of 30 μm. Ar was used as a shielding gas during fabrication.

The coupons and flat specimens underwent multiple steps of HT, including hot isostatic pressing (HIP) and T6 treatment (solutionizing, quenching, and artificial aging) at different temperatures and durations to investigate their effects on micro-/defect-structure and tensile behavior. Six different HT schedules, following AMS 2770 [18], ASTM F3301-18a [19], and ASTM B918/B918M [20] standards, were shortlisted, encompassing different combinations of HIP, solutionizing, and aging. The six sets of HT conditions are listed in **Table 2**.

Table 2. Different HT conditions studied in this study.

Condition	**HIP**	**Solutionizing**	**Aging**
Set 1: HIP+T6-1	510 °C/ 100 MPa/ 2 h	530 °C/ 2 h/ GQ	180 °C/ 8 h/AC
Set 2: HIP+T6-2	510 °C/ 100 MPa/ 2 h	530 °C/ 2 h/ GQ	160 °C/ 18 h/AC
Set 3: HIP+T6-3	510 °C/ 100 MPa/ 2 h	530 °C/ 2 h/ GQ	160 °C/ 34 h/AC
Set 4: HIP+T6-4	510 °C/ 100 MPa/ 2 h	515 °C/ 2 h/ GQ	160 °C/ 18 h/ AC
Set 5: HIP+T6-5	510 °C/ 100 MPa/ 2 h	500 °C/ 1.5 h/ GQ	165 °C/ 18 h/ AC
Set 6: T6-5	No HIP	500 °C/ 1.5 h/ GQ	165 °C/ 18 h/ AC

*GQ – Glycol quench, AC – Air cooled

Microstructural characterization of L-PBF A6061-RAM2 coupons from each HT set was conducted on the longitudinal plane (LP), which is parallel to the build direction. Metallography procedures followed ASTM E3 standard [21], including cold mounting, grinding with SiC sandpapers (grits sizes: 320 to 4000), and polishing to a mirror-finished surface using polishing cloths and colloidal silica (0.05 μm). Microstructural analysis was performed using a Zeiss 550 scanning electron microscope (SEM) equipped with electron backscattered diffraction (EBSD) and energy dispersive spectroscopy (EDS) detectors. EBSD maps were used to analyze grain size, while electron contrast channeling imaging technique generated backscattered electron (BSE) micrographs.

X-ray computed tomography (X-CT) was conducted on cylindrical coupons obtained from each HT set, each measuring 5 mm in diameter and 5 mm in height. These coupons were machined from the initially fabricated cylindrical bars to evaluate the volumetric defect contents in different

HT conditions. Scanning was carried out using a Zeiss Xradia 620 Versa system operating at 60 kV accelerating voltage and 6.5 W power, and producing images with a voxel size of 5.3 µm. The reconstructed images were analyzed using Zeiss proprietary software, followed by further analysis using ImageJ and Dragonfly software.

The tensile specimens were designed and tested based on the ASTM E8 standard [22]. The final geometry of tensile test specimens is shown in **Figure 1**. The tests were performed at a strain rate of 0.005 mm/mm/min. An extensometer was used to measure the axial strain and determine the modulus of elasticity and yield strength of the specimens until they reached a strain of 0.035 mm/mm. Once this limit was reached, the extensometer was removed due to its limited range, and the tests continued under displacement control until the specimens fractured completely. At least three specimens were tested at room temperature for each heat treatment set, and the average values of tensile properties, i.e., yield strength (YS), ultimate tensile strength (UTS), and elongation to failure (EL), were recorded and reported. After fracture, the surfaces were examined using SEM to study the fracture mechanisms.

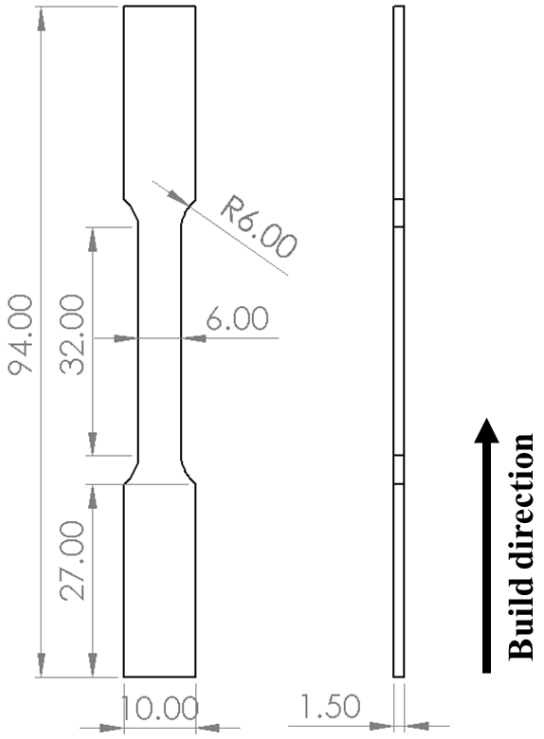

Figure 1. Geometry of L-PBF A6061-RAM2 tensile test specimen following ASTM E8. Note that all the dimensions are in 'mm'.

Results and Discussion

The inverse pole figure (IPF) maps obtained from EBSD analysis of L-PBF A6061-RAM2 specimens in non-heat treated (NHT) and different HT conditions are presented in **Figure 2**. The IPF maps depicted the grain structure on the LP, showing equiaxed grains for both NHT and different HT conditions. The average grain sizes (measured in equivalent circle diameter) were consistent across all HT conditions, ranging from 0.4 ~ 0.6 µm. The presence of inoculant particles facilitated grain refinement and the formation of fine equiaxed grains during solidification. However, the secondary phase particles precipitating during solidification persisted even after different HT conditions. Therefore, the overall grain structure remained consistent for all HT conditions. The grain size distribution presented in **Figure 2(h)** shows that, in all HT conditions, the majority of grains were predominantly below 1 µm in size. Additionally, the grain counts in the [0 – 1) µm size interval appeared to have increased with the duration of aging, ranging from 8 hrs to 34 hrs (see **Figure 2(h)**).

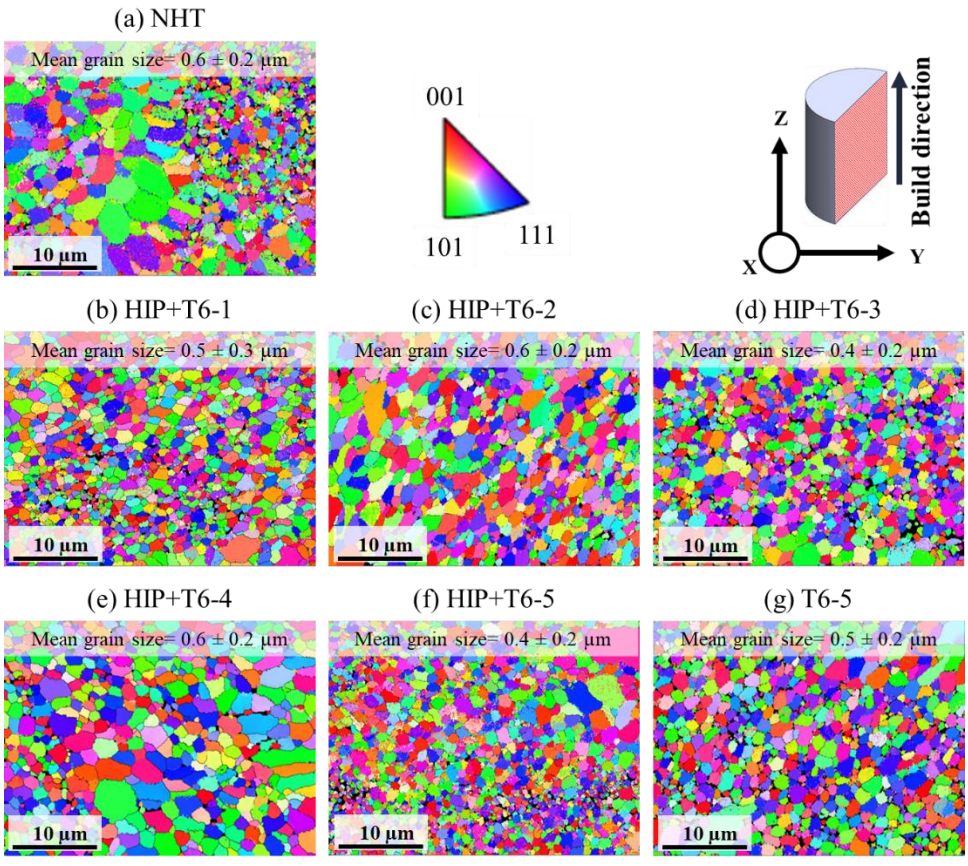

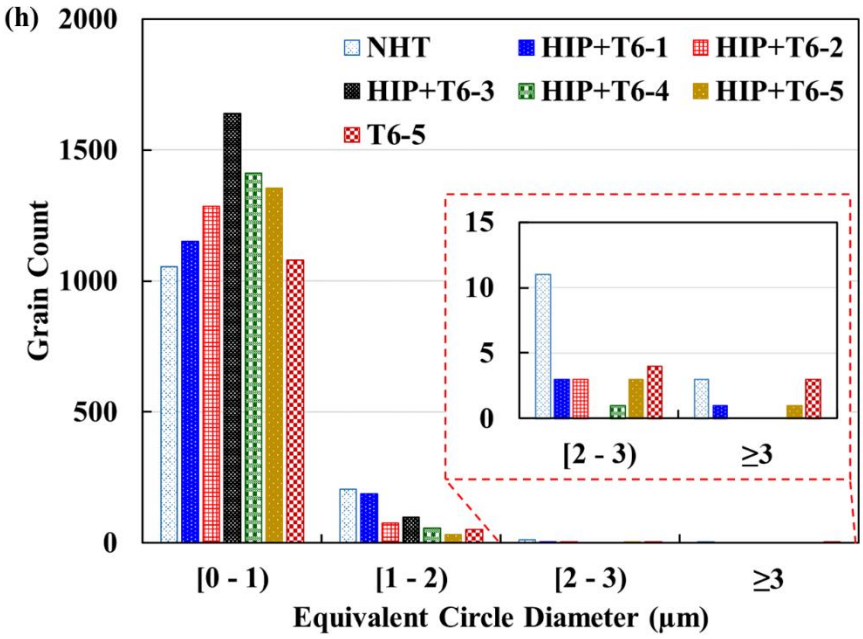

Figure 2. The IPF maps obtained from EBSD analysis for L-PBF A6061-RAM2 alloy in different HT conditions: (a) NHT, (b) HIP+T6-1, (c) HIP+T6-2, (d) HIP+T6-3, (e) HIP+T6-4, (f) HIP+T6-5, (g) T6-5. (h) The grain size distribution in different HT conditions.

The BSE micrographs of A6061-RAM2 alloy in NHT and different HT conditions of the LP are presented in **Figure 3**. The secondary phase particles, such as TiC and B_4C, were observed randomly distributed throughout the microstructure at lower magnifications. These particles remained stable for all HT conditions. At higher magnifications, finer Ti-Si intermetallic precipitates, likely Ti_5Si_3, were observed along the grain boundaries in the NHT condition (see **Figure 3** (c)). Following the T6 treatment under various HT conditions, Mg_2Si is typically expected to precipitate along the grain boundaries of the A6061 alloy [23]. The coarsening of these Mg_2Si particles appears to increase with aging duration, with the HIP+T6-3 condition exhibiting the coarsest particles (see **Figure 3** (l)). Microcracks and volumetric defects were visible in the microstructure under NHT and T6-5 conditions (see **Figure 3** (a)-(c) and (s)-(u)).

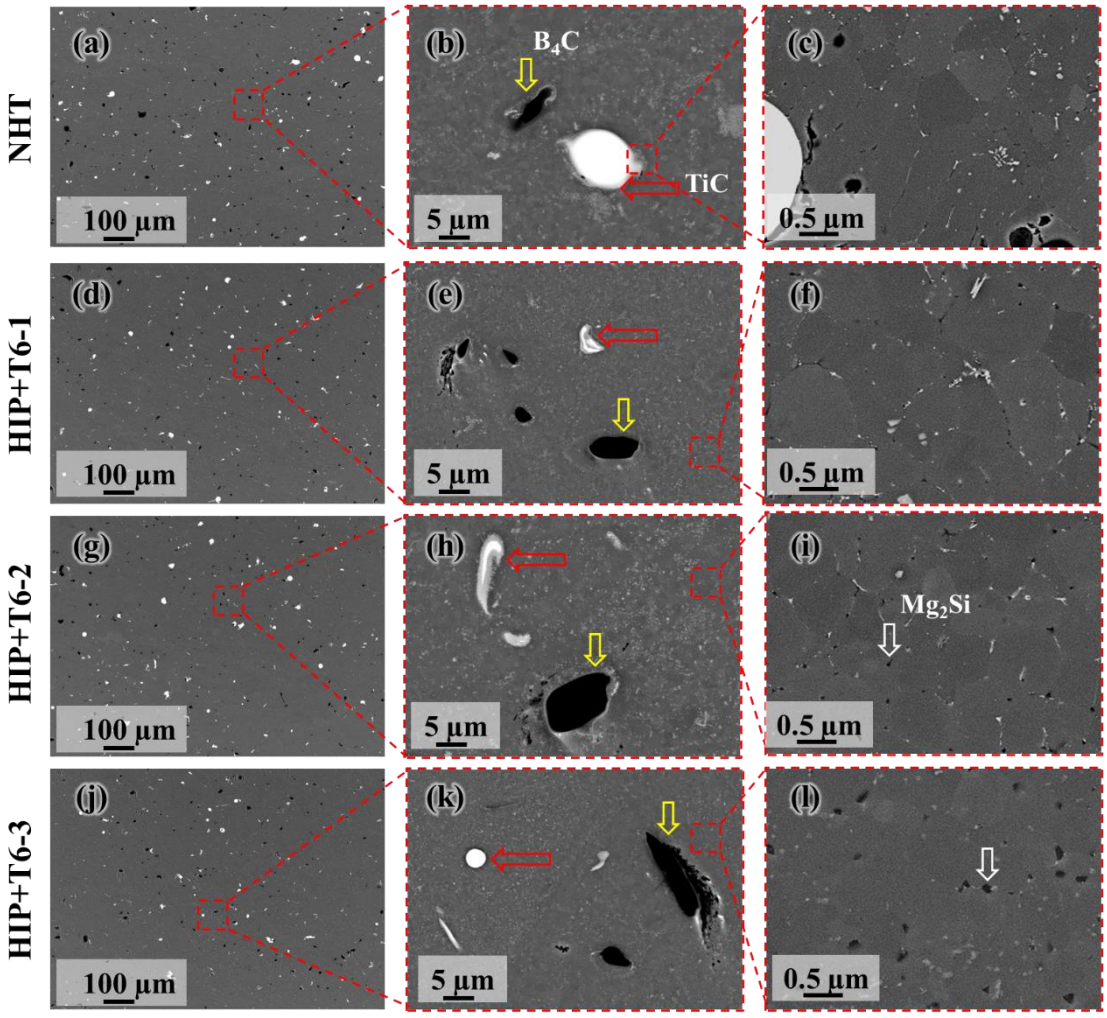

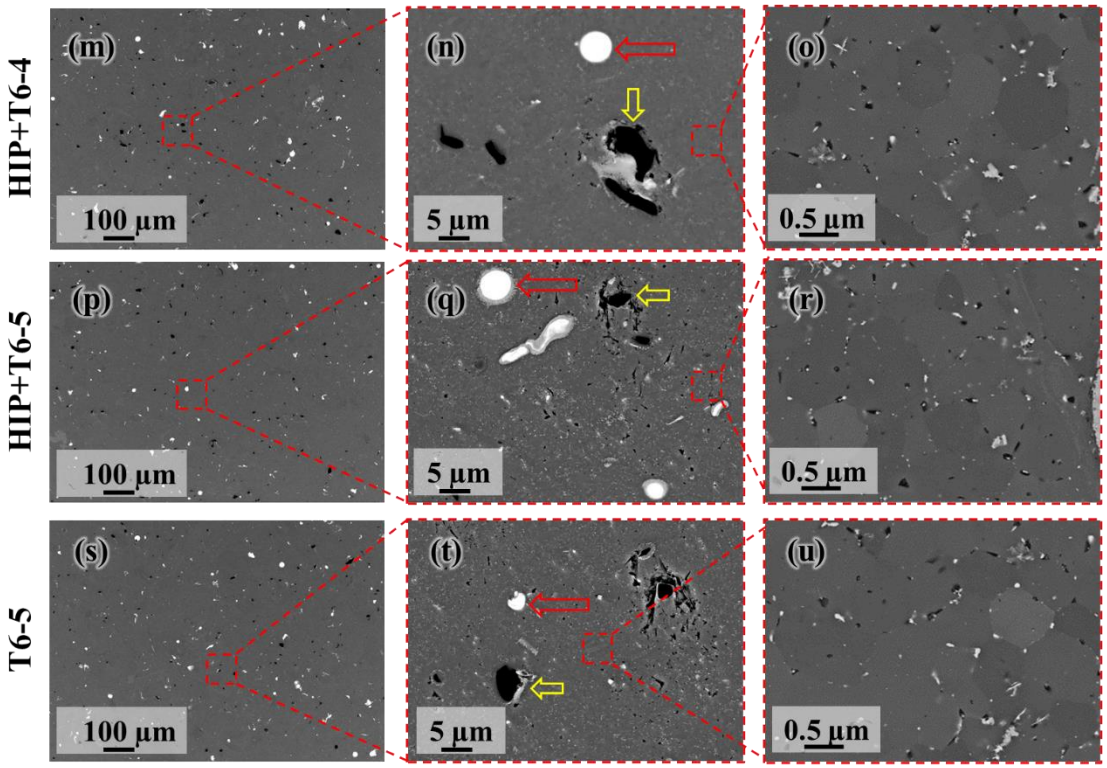

Figure 3. The BSE images in three magnifications for L-PBF A6061-RAM2 alloy in different HT conditions: (a)-(c) NHT, (d)-(f) HIP+T6-1, (g)-(i) HIP+T6-2, (j)-(l) HIP+T6-3, (m)-(o) HIP+T6-4, (p)-(r) HIP+T6-5, and (s)-(u) T6-5.

The EDS elemental maps presented in **Figure 4** for the HIP+T6-2 condition confirm the presence of TiC, B_4C, and Ti_5Si_3 secondary phase particles. However, the Mg_2Si particles might be too fine to be clearly detected due to the resolution limitations of the EDS.

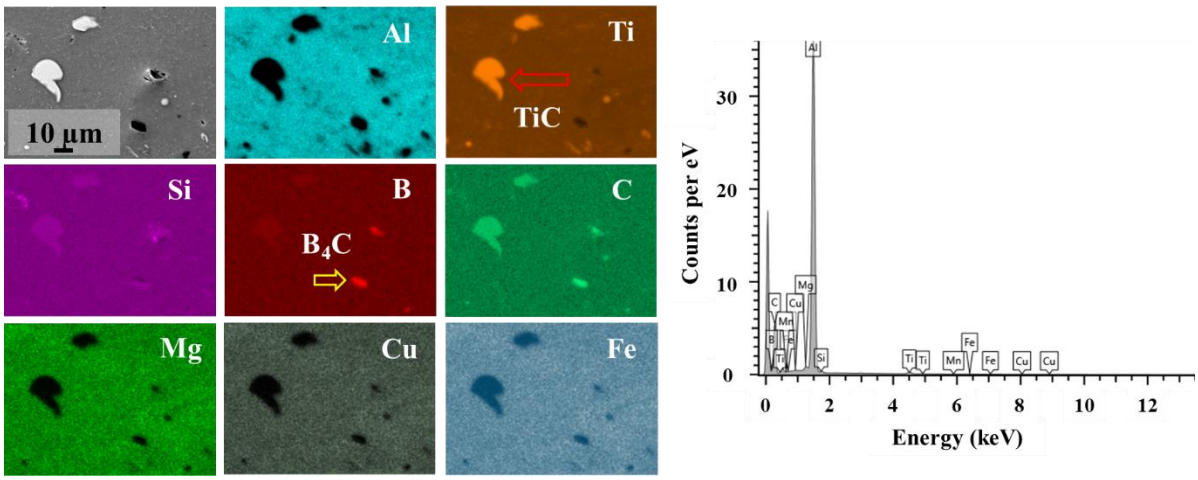

Figure 4. Results from EDS analysis, the elemental maps for L-PBF A6061-RAM2 alloy in HIP+T6-2 condition.

The defect content within the X-CT scanned coupons in NHT, HIP+T6-2, and T6-5 conditions are presented in Figure 5 (a)-(c). The HIP+T6-2 treated coupon was selected and reported here, as a representation of all HIP incorporating HT conditions. The histograms for the defect size distribution are presented in Figure 5 (d), where defect counts are divided by the total scanned volume. The relative porosity of the coupon in NHT was 0.09% with the largest defect size of 98 µm. HIP including HT greatly reduced the volumetric defects size and population with the largest defect size of 37 µm. However, only the T6-treated HT without HIP in the T6-5 condition showed a relative porosity of 0.11% with the largest defect size of 111 µm.

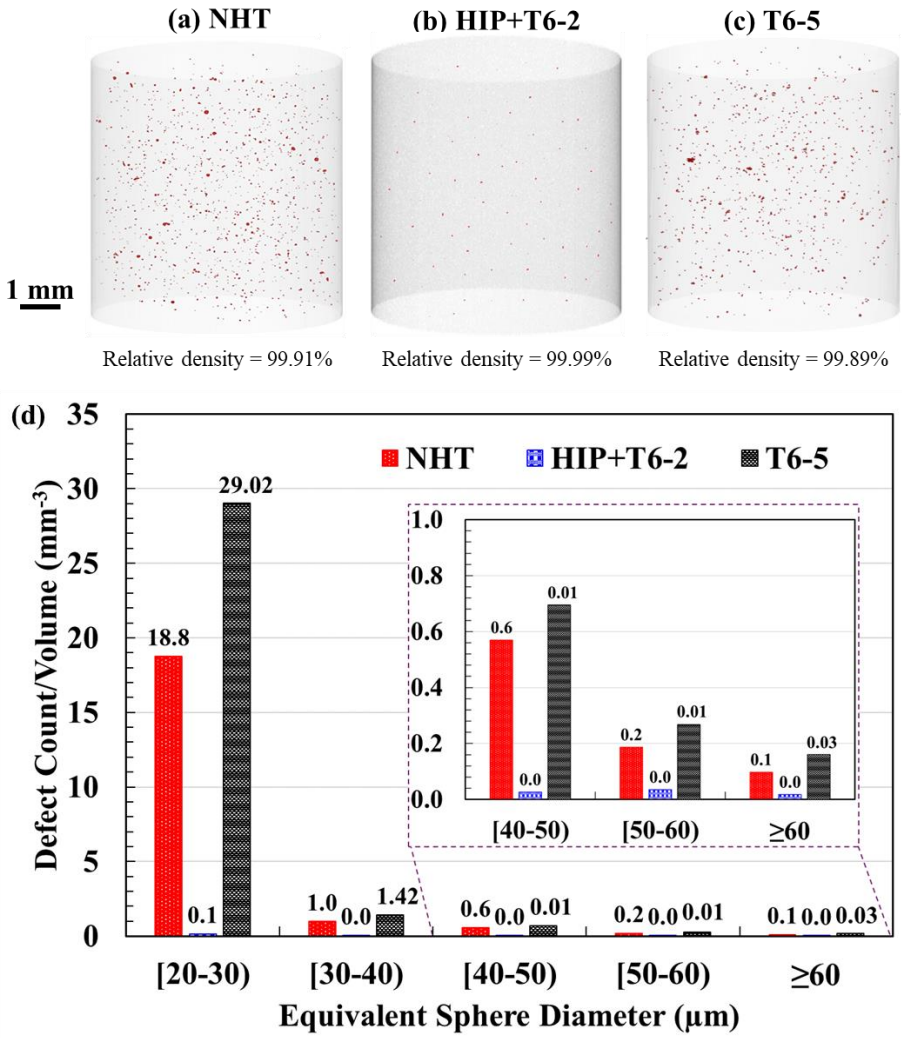

Figure 5. X-CT scan results for L-PBF A6061-RAM2 coupons in NHT, HIP+T6-2, and T6-5 conditions presented using (a)-(c) 3D visualization and (d) defect size distributions.

The engineering stress-displacement curves and quasi-static tensile properties, including yield strength (YS), ultimate tensile strength (UTS), and elongation to failure (EL) of L-PBF A6061-RAM2 specimens in different HT conditions are presented in **Figure 6** (a) and (b), respectively. These properties were compared with those of wrought A6061-T6 [24] and L-PBF A6061-T6 (without RAM) [25]. L-PBF A6061-RAM2 alloy exhibited higher YS and UTS compared to wrought and L-PBF A6061-T6 alloy. This can be attributed to its finer grain structure of L-PBF A6061-RAM2 alloy, which makes intergranular dislocation storage more difficult due to dislocation starvation. Yielding is primarily governed by dislocation emission from grain boundaries, leading to higher strengths [26][27]. However, the YS increased with the aging duration due to the size and population increase of Mg_2Si precipitates through the precipitation strengthening mechanism (see **Figure 3**) [28]. The engineering stress-displacement curves in **Figure 6** demonstrate a yield point phenomenon for all HT conditions. This is suspected to be caused by the pinning and unpinning of dislocations due to the limited solid solution of Ti, Cu, and C atoms, creating a Cottrell atmosphere around the dislocations [29]. The elastic field interaction between these atoms and the moving dislocations limits their free motions, causing dislocation pinning. As straining continues, the dislocations are released, leading to a sudden drop in stress until they are pinned again by the solid solution of these atoms. EL was slightly lower for L-PBF A6061-RAM2 than wrought A6061-T6 but significantly higher than L-PBF A6061-T6 (without RAM). The tensile fracture surfaces of the specimens are shown in **Figure 7**, revealing similar fracture mechanisms across different HT conditions. L-PBF A6061-RAM2 specimens in all HIP-included HT conditions exhibited comparable EL, except for the T6-5 condition without HIP, which showed slightly lower EL due to more volumetric defects detected by the X-CT scan (see **Figure 5**).

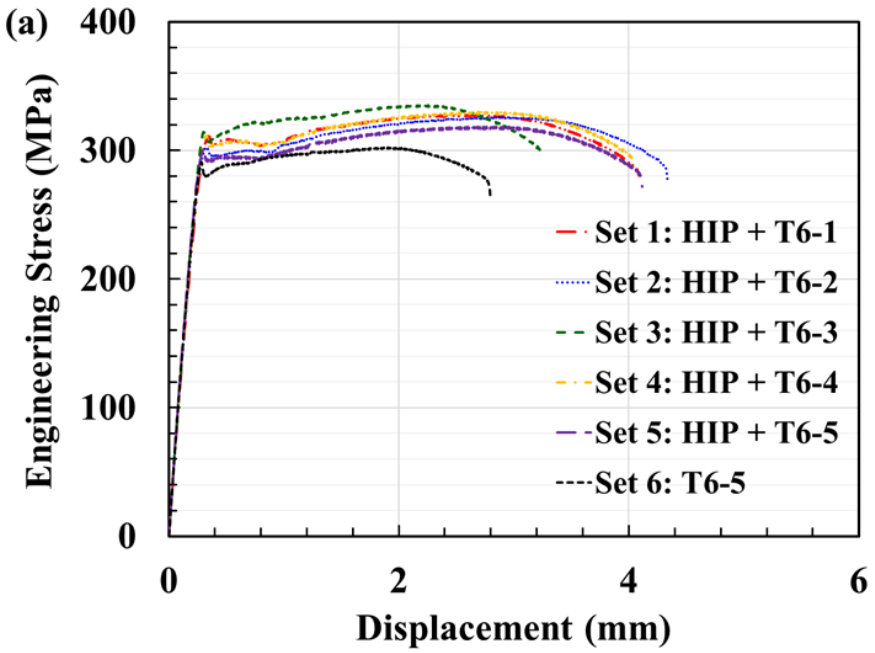

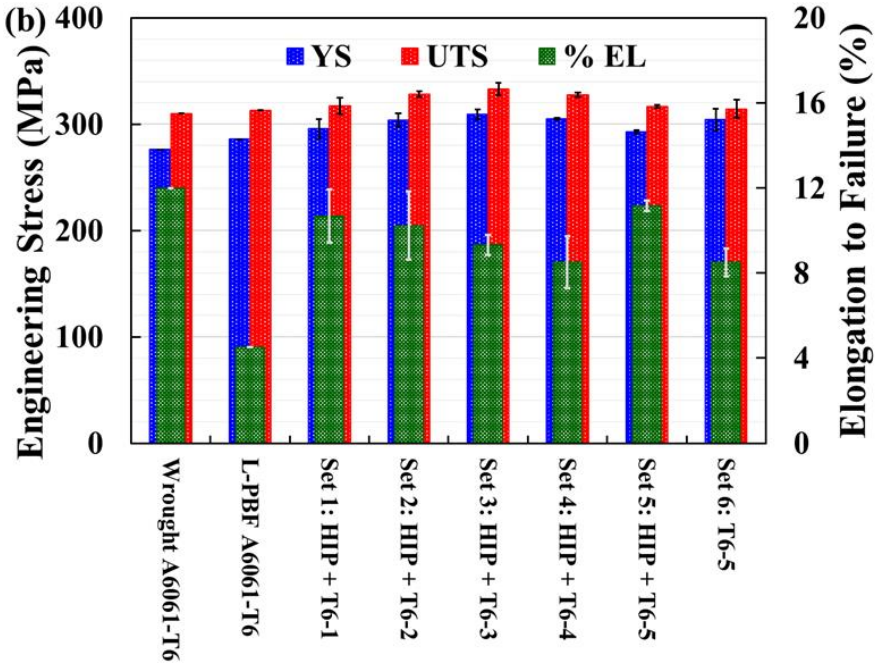

Figure 6. Tensile behavior of L-PBF A6061-RAM2 alloy in different HT conditions: (a) engineering stress-displacement curves, and (b) comparative bar charts for tensile properties of L-PBF A6061-RAM2 obtained in this study, and those of wrought A6061-T6 [24], and L-PBF A6061-T6 [25] from the literature.

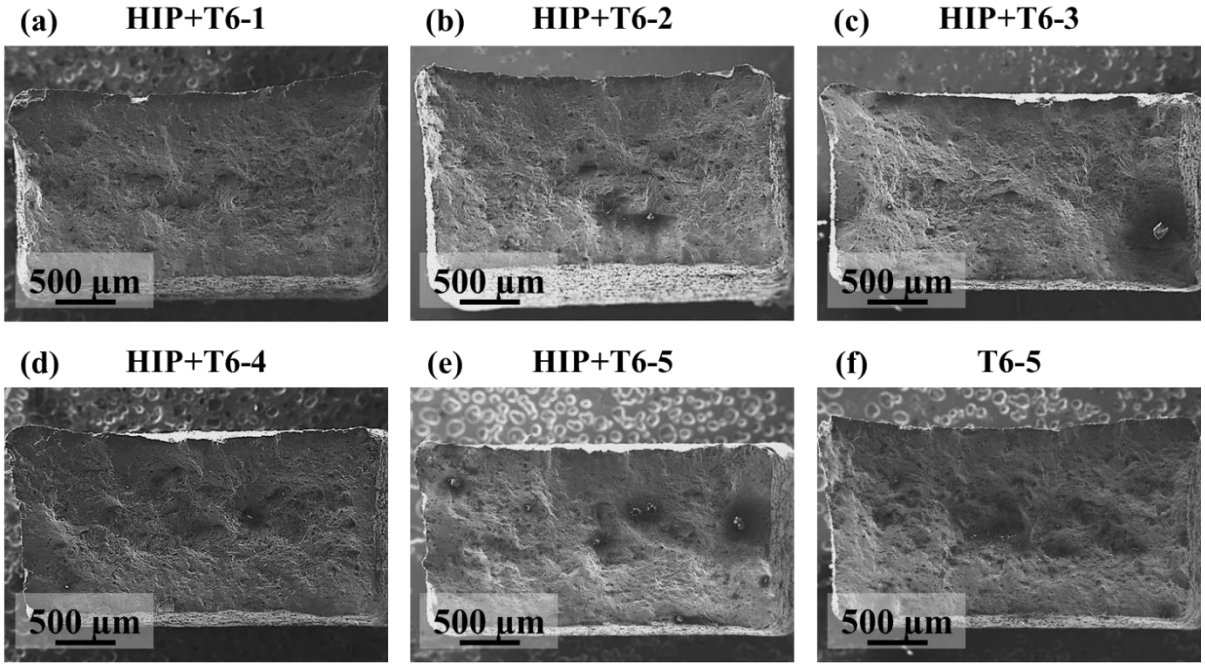

Figure 7. The tensile fracture surfaces of L-PBF A6061-RAM2 specimens in different HT conditions.

Conclusions

This study investigated the effect of heat treatment (HT) on the micro-/defect-structure and room temperature tensile behaviors of A6061-RAM2 fabricated using laser powder bed fusion. The following conclusions were drawn:

1. The inoculant particles, such as TiC and B_4C, aided in grain refinement and the formation of fine equiaxed grains during solidification. However, secondary phase particles precipitated during solidification persisted in all HT conditions, leading to a consistent overall grain structure.
2. All HTs incorporating hot isostatic pressing significantly reduced the volumetric defects.
3. Tensile strength increased with aging duration, likely due to the growth in size and population of Mg_2Si precipitates through the precipitation strengthening mechanism.

Acknowledgments

This research is based upon the work partially funded by the National Aeronautics and Space Administration (NASA) contract 80MSFC19C0010 and the National Science Foundation (NSF) under grant No. 2319690. A portion of this work was carried out at the Jet Propulsion Laboratory, California Institute of Technology, under a contract with the NASA (80NM0018D0004). Reference herein to any specific commercial product, process, or service by trade name, trademark, manufacturer, or otherwise, does not constitute or imply its endorsement by the United States Government or the Jet Propulsion Laboratory, California Institute of Technology. The team would like to thank the Elementum 3D team for various technical discussions on this alloy. This paper describes objective technical results and analysis. Any subjective views or opinions that might be expressed in the paper do not necessarily represent the views of the NASA or the United States Government.

References

[1] Lakshminarayanan AK, Balasubramanian V, Elangovan K. Effect of welding processes on tensile properties of AA6061 aluminium alloy joints. Int J Adv Manuf Technol 2009;40:286–96. https://doi.org/10.1007/s00170-007-1325-0.

[2] Sharma VK, Kumar V, Joshi RS. Investigation of rare earth particulate on tribological and mechanical properties of Al-6061 alloy composites for aerospace application. J Mater Res Technol 2019;8:3504–16. https://doi.org/10.1016/j.jmrt.2019.06.025.

[3] Sanders RE. Technology innovation in aluminum products. JOM 2001;53:21–5. https://doi.org/10.1007/s11837-001-0115-7.

[4] Khan MF, Nezhadfar PD, Gradl PR, Godfrey D, Diemann J, Shao S, et al. Investigate the height dependency of the micro-/defect-structure and mechanical properties of additively manufactured AlF357 aluminum alloy. Int. Solid Free. Fabr. Symp., 2022, p. 302–13.

https://doi.org/10.26153/tsw/44148.

[5] Ding Y, Muñiz-Lerma JA, Trask M, Chou S, Walker A, Brochu M. Microstructure and mechanical property considerations in additive manufacturing of aluminum alloys. MRS Bull 2016;41:745–51. https://doi.org/10.1557/mrs.2016.214.

[6] Martin JH, Yahata BD, Hundley JM, Mayer JA, Schaedler TA, Pollock TM. 3D printing of high-strength aluminium alloys. Nature 2017;549:365–9. https://doi.org/10.1038/nature23894.

[7] Mehta A, Zhou L, Huynh T, Park S, Hyer H, Song S, et al. Additive manufacturing and mechanical properties of the dense and crack free Zr-modified aluminum alloy 6061 fabricated by the laser-powder bed fusion. Addit Manuf 2021;41:101966. https://doi.org/10.1016/j.addma.2021.101966.

[8] Sonawane A, Roux G, Blandin J-J, Despres A, Martin G. Cracking mechanism and its sensitivity to processing conditions during laser powder bed fusion of a structural aluminum alloy. Materialia 2021;15:100976. https://doi.org/10.1016/j.mtla.2020.100976.

[9] Cross CE. On the Origin of Weld Solidification Cracking. In: Böllinghaus T, Herold H, editors. Hot Crack. Phenom. Welds, Berlin/Heidelberg: Springer-Verlag; 2005, p. 3–18. https://doi.org/10.1007/3-540-27460-X_1.

[10] Cicală E, Duffet G, Andrzejewski H, Grevey D, Ignat S. Hot cracking in Al–Mg–Si alloy laser welding – operating parameters and their effects. Mater Sci Eng A 2005;395:1–9. https://doi.org/10.1016/j.msea.2004.11.026.

[11] Kou S. A simple index for predicting the susceptibility to solidification cracking. Weld J 2015;94:374–88.

[12] Uddin SZ, Murr LE, Terrazas CA, Morton P, Roberson DA, Wicker RB. Processing and characterization of crack-free aluminum 6061 using high-temperature heating in laser powder bed fusion additive manufacturing. Addit Manuf 2018;22:405–15. https://doi.org/10.1016/j.addma.2018.05.047.

[13] Kou S. Predicting Susceptibility to Solidification Cracking and Liquation Cracking by CALPHAD. Metals (Basel) 2021;11:1442. https://doi.org/10.3390/met11091442.

[14] Liu J, Wu Y, Kou S. Roles of tension and solidification shrinkage in solidification cracking during aluminium arc welding. Sci Technol Weld Join 2021;26:614–21. https://doi.org/10.1080/13621718.2021.1985368.

[15] Mertens AI, Lecomte-Beckers J. On the Role of Interfacial Reactions, Dissolution and Secondary Precipitation During the Laser Additive Manufacturing of Metal Matrix Composites: A Review. In: Shishkovsky I V, editor. New Trends 3D Print., Rijeka: InTech; 2016. https://doi.org/10.5772/63045.

[16] Xie X, Ma Y, Chen C, Ji G, Verdy C, Wu H, et al. Cold spray additive manufacturing of metal matrix composites (MMCs) using a novel nano-TiB2-reinforced 7075Al powder. J Alloys Compd 2020;819:152962. https://doi.org/https://doi.org/10.1016/j.jallcom.2019.152962.

[17] Lee W-S, Tang Z-C. Relationship between mechanical properties and microstructural response of 6061-T6 aluminum alloy impacted at elevated temperatures. Mater Des 2014;58:116–24. https://doi.org/10.1016/j.matdes.2014.01.053.

[18] SAE Aerospace. AMS2770: Heat Treatment of Wrought Aluminum Alloy Parts. Aerosp Mater Specif AMS2770 2011;Rev. J.

[19] ASTM F3301-18a. Standard for Additive Manufacturing – Post Processing Methods – Standard Specification for Thermal Post-Processing Metal Parts Made Via Powder Bed Fusion. ASTM Stand 2018:3. https://doi.org/10.1520/F3301-18A.2.

[20] ASTM International. ASTM B918/B918M : Standard Practice for Heat Treatment of Wrought Aluminum Alloys. West Conshohocken, PA 19428-2959 USA 2001.

[21] ASTM International. ASTM E3: Standard Guide for Preparation of Metallographic Specimens. West Conshohocken, PA 19428-2959 USA 2012;03.01:1–12. https://doi.org/10.1520/E0003-11R17.

[22] ASTM International. ASTM E8/E8M Standard test methods for tension testing of metallic materials. West Conshohocken, PA 19428-2959 USA 2013. https://doi.org/10.1520/E0008.

[23] Kahlenberg R, Wojcik T, Falkinger G, Krejci AL, Milkereit B, Kozeschnik E. On the precipitation mechanisms of β-Mg2Si during continuous heating of AA6061. Acta Mater 2023;261:119345. https://doi.org/10.1016/j.actamat.2023.119345.

[24] ASM International Handbook Committee. ASM Handbook Vol. 2: Properties and Selection: Nonferrous Alloys and Special-Purpose Materials. 2001.

[25] Uddin SZ, Murr LE, Terrazas CA, Morton P, Roberson DA, Wicker RB. Processing and characterization of crack-free aluminum 6061 using high-temperature heating in laser powder bed fusion additive manufacturing. Addit Manuf 2018;22:405–15. https://doi.org/10.1016/j.addma.2018.05.047.

[26] Pande CS, Cooper KP. Nanomechanics of Hall–Petch relationship in nanocrystalline materials. Prog Mater Sci 2009;54:689–706. https://doi.org/10.1016/j.pmatsci.2009.03.008.

[27] Yang C, Liu Z, Zheng Q, Cao Y, Dai X, Sun L, et al. Ultrasound assisted in-situ casting technique for synthesizing small-sized blocky Al3Ti particles reinforced A356 matrix composites with improved mechanical properties. J Alloys Compd 2018;747:580–90. https://doi.org/10.1016/j.jallcom.2018.02.010.

[28] Linardi E, Haddad R, Lanzani L. Stability Analysis of the Mg2Si Phase in AA 6061 Aluminum Alloy. Procedia Mater Sci 2012;1:550–7. https://doi.org/10.1016/j.mspro.2012.06.074.

[29] Avateffazeli M, Carrion PE, Shachi-Amirkhiz B, Pirgazi H, Mohammadi M, Shamsaei N, et al. Correlation between tensile properties, microstructure, and processing routes of an Al–Cu–Mg–Ag–TiB2 (A205) alloy: Additive manufacturing and casting. Mater Sci Eng A 2022;841:142989. https://doi.org/10.1016/j.msea.2022.142989.